

## Neutron Scattering by Rotons in Liquid Helium<sup>†</sup>

O. W. Dietrich\*

*Danish Atomic Energy Commission, Research Establishment Risø, Roskilde, Denmark*

and

E. H. Graf\* and C. H. Huang\*

*State University of New York, Stony Brook, New York 11790*

and

L. Passell

*Brookhaven National Laboratory, Upton, New York 11973*

(Received 27 August 1971)

The elementary excitations in superfluid helium have been studied in the wave-vector range  $1.5 < Q < 2.3 \text{ \AA}^{-1}$  by inelastic neutron scattering. The single-excitation scattering function  $S_1(Q, \hbar\omega)$  was measured for pressures between 1 atm and the solidification pressure and for temperatures from 1.3°K to above the transition temperature  $T_\lambda$ . The dispersion curves were fitted to parabolas and the appropriate Landau parameters tabulated vs temperature and pressure. By accounting for the effect of the instrumental resolution it was possible to observe a line broadening at low temperatures which sets in when the slope of the dispersion curve equals the sound velocity. There are strong indications that this is due to the roton-phonon interaction proposed by Pitaevskii. The line broadening observed when the temperature approaches  $T_\lambda$  is well accounted for by the roton-roton interaction as calculated by Landau and Khalatnikov. The results have been related through thermodynamics to other properties of the liquid and the spectral form of the excitations compared to those observed in magnetic systems close to the critical temperature.

### I. INTRODUCTION

The first direct evidence of elementary excitations in liquid helium was provided by neutron-scattering experiments.<sup>1-3</sup> These experiments also showed that the single-excitation dispersion curve closely follows the form envisioned by Landau<sup>4</sup>: an essentially linear "phonon" region at small momentum transfers and at larger momentum transfers a "roton" region in which the curve exhibits a characteristic parabolic form. Today, the major features of the low-temperature dispersion curve at the saturated vapor pressure are well established and more emphasis is being placed on detailed studies of the neutron scattering at large and small momentum transfers.<sup>5</sup> The recently discovered multiphonon branch of the dispersion curve observed at higher energies<sup>5</sup> is also attracting considerable attention.

Despite a substantial and long-continued experimental effort, however, there are still gaps in our knowledge of the properties of the excitations of this unusual liquid. This is particularly true at pressures above the saturated vapor pressure where there is at present only a single neutron-scattering measurement at 1.1°K and 25.3 atm.<sup>6</sup> To fill part of this gap we have recently made an extended series of neutron-scattering measurements on liquid helium under pressure. These measurements, taken together, constitute a systematic study of the

roton region of the dispersion curve in the pressure range between 1 atm and the solidification pressure. Almost all of the data were taken in the superfluid region at temperatures above 1.3°K; in a few cases measurements were also made in the normal-fluid region above the transition temperature  $T_\lambda$ . We believe the results provide a reasonably complete description of the roton parameters (i. e., the energy gap, effective mass, and the wave number corresponding to the position of the roton minimum) over the entire superfluid region above 1.3°K.

A secondary aim of this study has been to investigate the form of the neutron interaction cross section—the "line shape." This involved correcting the observed line shapes for the effects of instrumental resolution and the Boltzmann factor (which governs the relative intensities of absorptive and emissive scattering processes). Thus, the energies and widths of the lines become representations of the actual line shapes or, in other words, the spectral form of the excitations. As we will show, the line shapes near  $T_\lambda$  are remarkably similar to those observed in other critical systems.

The paper is organized as follows: Apparatus and measuring procedures are discussed in Sec. II. Section III is devoted to data analysis and includes a description of the Monte Carlo technique used to determine the instrumental resolution function. Experimental results are presented in Sec. IV and are discussed and related to the thermodynamic properties of the liquid in Sec. V.

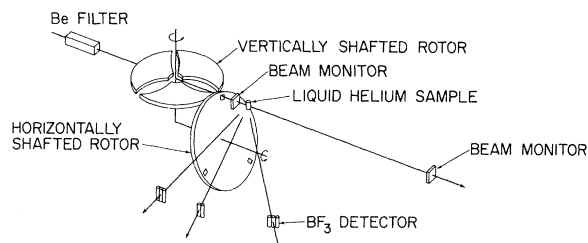


FIG. 1. Schematic representation of the slow chopper and time-of-flight spectrometer.

## II. APPARATUS

### A. Neutron Spectrometer

All of the measurements were made with the slow neutron chopper and the time-of-flight spectrometer shown schematically in Fig. 1. The chopper follows the design of Otnes and Palevsky<sup>7</sup> and is of the two-rotor type. The first rotor is 80 cm in diam and serves both as chopper and monochromator. Three curved channels are contained within the plane of its wheel. They are 1.27 cm wide at entrance and exit and are set 120° apart. As can be seen from the figure, the axis of this rotor is vertical. The second rotor functions simply as a chopper. Like the first rotor, it is 80 cm in diam, but the axis is horizontal. It contains three slots 1.27 cm wide set at 120° intervals in the periphery of the wheel. The pair of wheels rotate in phase and in a sense that the slots travel in opposite directions at their point of closest approach. This is also the point at which they intersect the beam. Both the speed of rotation and the phase angle between rotors are electronically controlled, the rotor speeds to better than 1 part in 1200 and the phase angle to 1 part in 800.

Since the system is specifically intended for *cold* neutron spectrometry, a 30-cm-long polycrystalline beryllium filter is installed in the incident beam to eliminate fast and thermal neutrons which would otherwise act as sources of unwanted background. Accordingly, the operating range of the device is limited by the filter to energies less than 5 meV. Maximum intensity is obtained at 4.83 meV corresponding to a rotational velocity of 12 200 rpm. At this speed, used for all our measurements, the neutron burst at the sample located 35.5 cm from the second rotor had a width of 26  $\mu$ sec and an energy spread  $\Delta E/E$  of about 0.07. Horizontal and vertical divergences of the beam were, respectively, 0.88° and 1.64°. Beam width at the sample was 1.27 cm and beam height 5 cm.

A conventional time-of-flight spectrometer was used to determine the energies of the neutrons scattered by the sample. It employs 14 cylindrical  $\text{BF}_3$  detectors of 2.4 cm i. d. and with an active

length of approximately 15 cm. Referring to Fig. 1, the detectors are located on an arc (radius 177 cm) and mounted with their axes vertical. Thus oriented they subtend in the horizontal plane an angle of 1° as viewed from the sample position. The enriched  $\text{BF}_3$  gas pressure in the detectors is roughly 1.7 atm. At this pressure the linear absorption coefficient of the gas is about  $0.36 \text{ cm}^{-1}$  for 4.83-meV neutrons.

All detectors feed to a central time-delay analyzer which operates with 256 time channels, each of 8- $\mu$ sec duration. Altogether the time interval spanned is 2048  $\mu$ sec which more than covers the 1640  $\mu$ sec interval between neutron bursts.

The incident beam energy is determined by measuring the time of flight between a pair of beam monitors, one located 15 cm in front of the sample, the other 177 cm beyond it. These monitors are also used to define "time zero," the time at which the incident neutron burst reaches the sample.

### B. Sample and Associated Systems

Figure 2 shows the arrangement of the liquid-helium sample and the associated cryogenics.

The sample cell was an aluminum cylinder 2.5 cm in diam and 7.7 cm high with walls 1.75 mm thick in the section traversed by the beam. A pair of cadmium spacers divided the sample cavity vertically into three sections to reduce the effects of multiple scattering.

The cell was attached to a 180-cm<sup>3</sup> capacity heli-

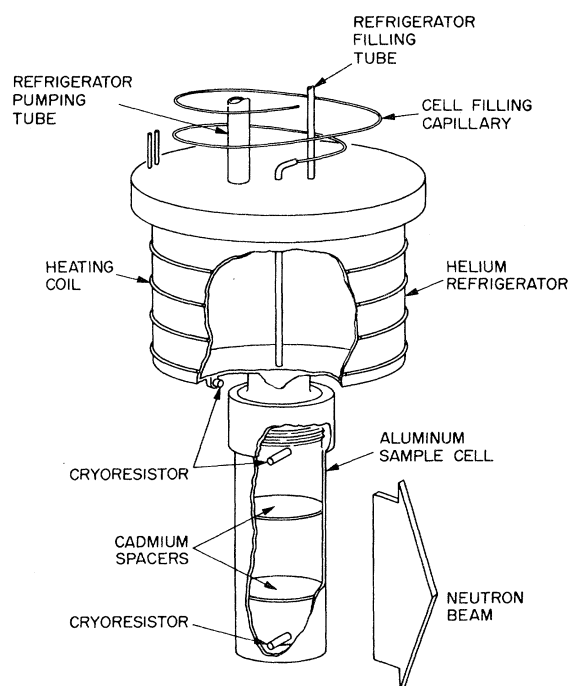


FIG. 2. Helium refrigerator and sample cell.

um refrigerator—a copper vessel suspended below the main 4.2°K liquid-helium bath. This refrigerator was connected to the bath by a capillary and an externally operated low-temperature valve so that it could be filled with liquid helium directly from the bath. By controlled pumping of the refrigerator, any temperature between 1.2 and 4.2°K could be maintained for periods in excess of 24 h.

Filling and emptying the sample cell was done by means of a tube passing through the helium refrigerator. A 100-cm-long section of 0.5-mm-i.d. Cu-Ni capillary was employed between the refrigerator and the 4.2°K bath, elsewhere 2.3-mm-i.d. tubing was used. The section of fine capillary was necessary to keep the heat leak to the refrigerator at a reasonable level when the sample cell was below the superfluid transition temperature.

All thermometry was done with Ge cryoresistors mounted inside the sample cell immediately above and below the beam. The cryoresistors were calibrated *in situ* to an absolute accuracy of  $\pm 0.005$ °K using the 1958 helium vapor-pressure scale. For measurements near  $T_\lambda$ , where a high degree of temperature stability was required, an ac bridge controller was used in combination with a small heating coil attached to the helium refrigerator. This proportional control system held temperature drift to less than  $\pm 0.002$ °K; otherwise when only controlled pumping was employed about  $\pm 0.02$ °K was maintained.

Pressure measurements were made at the top of the sample filling tube with a calibrated Bourdon pressure gauge. The accuracy of measurement was about  $\pm 0.14$  atm. Generally the drift in pressure during individual runs was of this order or slightly greater. However, both temperature and pressure were continuously monitored to be certain of stable conditions while data were being collected.

### III. DATA ANALYSIS

#### A. Instrumental Resolution

If the actual spectra are to be obtained from the observed line shapes it is necessary to take the instrumental resolution into account. To determine the resolution function for the chopper system described in Sec. II A, we used a computer “simulation” method based on the Monte Carlo technique.<sup>8</sup> Here we will briefly discuss the principle of the method and some of the more important features of the resolution function.

The conventional approach<sup>9-11</sup> to the determination of the resolution function of a neutron spectrometer involves analytical convolution of the transmission probabilities for the various parts of the instrument, such as collimators, Bragg reflecting crystals, chopper rotors, etc. This approach

has a number of shortcomings. First, the individual transmission probabilities have to be approximated by convenient functions (usually Gaussians) to make the convolution integrals tractable. Second, it is not easy to incorporate into the calculations the geometrical effects of detectors, samples, and crystals of finite size, a factor of particular importance in time-of-flight spectrometry. Finally, only the shape of the resolution function is determined. It has recently been pointed out that not only the shape but also the efficiency factor is needed<sup>12</sup> to properly unfold the experimental data. When conventional methods are employed, the calculation of the efficiency factor becomes a separate problem.

Our simulation method avoids all of these difficulties. Neither approximations of the transmission functions nor of the geometry are necessary. Individual neutrons are followed through the system with the Monte Carlo technique—the distribution functions for each part of the spectrometer operating in turn to select a statistically valid sample of the neutrons traversing the spectrometer. When the helium sample is simulated by an incoherent scatterer of the same geometry, but assuming a *fixed* energy transfer  $\hbar\omega$  for every scattering process, the neutrons “detected” by a simulated detector at a specified scattering angle map out exactly the instrumental resolution function  $R(\vec{Q} - \vec{Q}', \hbar\omega - \hbar\omega')$ . In this expression  $\vec{Q}$  is the average wave-vector transfer and is related, as is  $\hbar\omega$ , to the variables  $\vec{k}_i, E_i$  and  $\vec{k}_f, E_f$ , which are the wave vectors and energies of the incident and scattered neutrons, respectively. The relationship is expressed by the conservation equations  $\vec{Q} = \vec{k}_i - \vec{k}_f$  and  $\hbar\omega = E_i - E_f$ .

We have calculated the resolution function over the entire range of wave vector and energy transfers covered by our measurements and characterized its shape and efficiency by a set of empirical parameters. These parameters change significantly over the range of a single time-of-flight spectrum. This is illustrated in Fig. 3, where we show half-maximum contours in the  $(Q, \hbar\omega)$  plane at three representative points on the spectrum. Note that since we are dealing with a liquid, the usual four-dimensional space of the resolution function reduces to two dimensions, the wave-number transfer  $Q$ , and the energy transfer  $\hbar\omega$ .

#### B. Cross Section

The coherent neutron cross section per unit solid angle and energy interval for an isotropic sample of  $N$  atoms is given by the expression<sup>13</sup>

$$\frac{d^2\sigma}{d\Omega dE_f} = N \frac{k_f}{k_i} \frac{\sigma_c}{4\pi} s(Q, \hbar\omega), \quad (1)$$

where  $\sigma_c$  is the single-atom coherent cross section

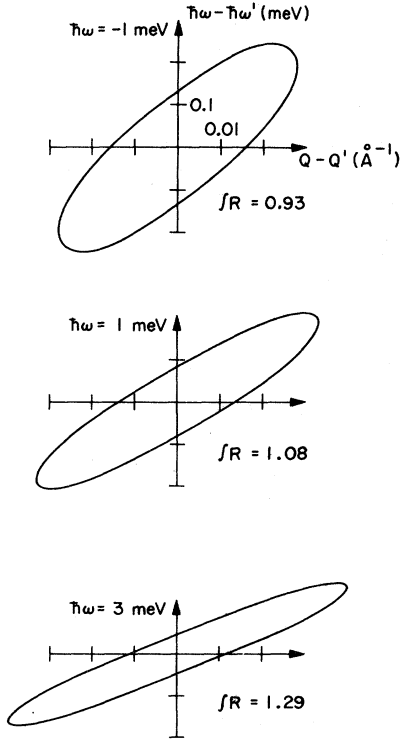


FIG. 3. Half-maximum contours of the resolution function for the time-of-flight spectrometer when operating with incident neutrons of 4.83-meV energy. The upper ellipse corresponds to 1-meV neutron energy gain and the middle and low ellipses to 1- and 3-meV energy loss, respectively. This is the range covered by a typical time-of-flight spectrum. Note the change of shape and the change in the efficiency of the spectrometer as given by the resolution volume  $\int R(Q', \hbar\omega') dQ' d(\hbar\omega')$ .  $fR$  given in the figure is normalized to give unit value for elastic scattering.

and the scattering function  $s(Q, \hbar\omega)$  is the Fourier transform of the density-density correlation function, i. e.,

$$s(Q, \hbar\omega) = \frac{1}{2\pi\hbar N} \int dt e^{-i\omega t} \int d\vec{r} e^{i\vec{Q}\cdot\vec{r}} \times \int d\vec{r}' \langle \rho(\vec{r}' - \vec{r}, 0) \rho(\vec{r}', t) \rangle. \quad (2)$$

When the density-density fluctuations on an atomic scale can be described by undamped plane waves (as is known to be the case in helium at low temperatures) the inelastic one-excitation part of the scattering function  $S_1(Q, \hbar\omega)$  becomes a  $\delta$  function in frequency

$$S_1(Q, \hbar\omega) = \frac{1}{2} \frac{\hbar\omega(Q)}{1 - e^{-\hbar\omega\beta}} C(Q) \times \{ \delta[\hbar\omega + \hbar\omega(Q)] + \delta[\hbar\omega - \hbar\omega(Q)] \}. \quad (3)$$

Here  $\hbar\omega(Q)$  is the dispersion relation for the excitations, and the two terms represent, respectively, annihilation- and creation-scattering processes.

As the temperature increases, however, the number of excitations also increases and interactions between them cause both line broadening and re-normalization of the energy. Ultimately (3) will no longer be valid. The problem is to find a form which properly describes the broadened line.

In practice, the actual line shape  $S_1(Q, \hbar\omega)$  cannot be directly deconvoluted from the data. Therefore, what is done is to start with an assumed form for  $S_1(Q, \hbar\omega)$  and fold it with the instrumental resolution function to obtain a simulated line shape which can be fitted to the data. The quality of the fit then indicates whether the chosen  $S_1(Q, \hbar\omega)$  satisfactorily describes the scattering process and therefore properly represents the spectral form of the excitation.

We assumed a line shape of Lorentzian form as suggested by Cohen.<sup>14</sup> This form was found to give statistically good fits to all our data. The actual expression used was

$$S_1(Q, \hbar\omega) = \frac{1}{2\pi} \frac{\hbar\omega}{1 - e^{-\hbar\omega\beta}} C(Q) \left\{ \frac{\hbar\Gamma(Q)}{\hbar^2\Gamma^2(Q) + [\hbar\omega + \hbar\omega(Q)]^2} + \frac{\hbar\Gamma(Q)}{\hbar^2\Gamma^2(Q) + [\hbar\omega - \hbar\omega(Q)]^2} \right\}, \quad (4)$$

where  $\hbar\Gamma(Q)$  is the half-width at half-maximum (HWHM). Note that (4) reduces to (3) in the limit when  $\hbar\Gamma(Q) \rightarrow 0$ .

### C. Unfolding Procedure

It is evident from Fig. 1 that the neutron detectors in a chopper spectrometer are fixed in space. Therefore the time-of-flight spectra are measurements at *fixed scattering angles* of the scattered intensities per unit *time-of-flight interval*. Since the cross section is expressed in terms of  $Q$  and  $\hbar\omega$ , the time-of-flight spectra must be transformed to these variables. Figure 4 shows how the points sampled in a typical time-of-flight spectrum transform to a curve (essentially a straight line) in the  $(Q, \hbar\omega)$ -coordinate system of the cross section. For reference, the corresponding scattering diagram is included as an insert in the figure.

The intensity measured in a time channel at time  $t$  by a detector at scattering angle  $\theta$  is related to the energy spectrum  $I_\theta(\hbar\omega)$  by the expression

$$I_\theta(t) = I_\theta(\hbar\omega) \frac{\partial(\hbar\omega)}{\partial t}, \quad (5)$$

where the Jacobian  $\partial(\hbar\omega)/\partial t = \text{const} \times k_f^3$  accounts for the transformation from a time to an energy scale.  $I_\theta(\hbar\omega)$  is given by folding the cross section with the instrumental resolution function, i. e.,

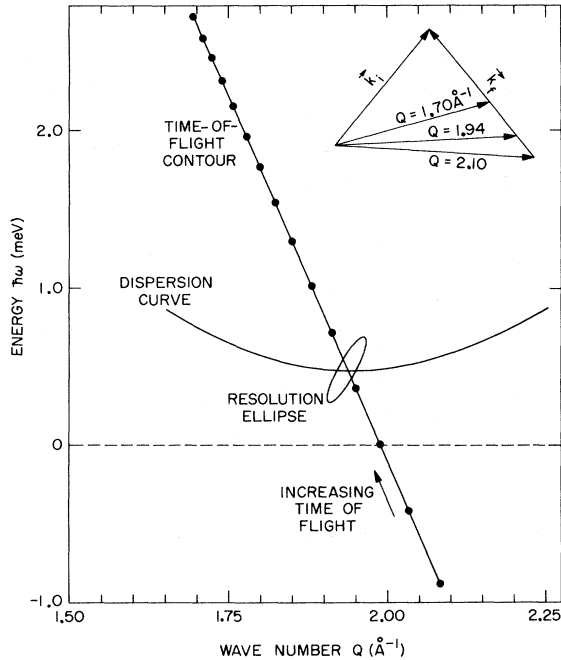


FIG. 4. Representation of a typical time-of-flight spectrum in a  $(Q, \hbar\omega)$  coordinate system. The rulings indicate equal time-of-flight intervals. The insert represents the scattering diagram.

$$I_{\theta}(\hbar\omega) = \int \left( \frac{d^2\sigma}{d\Omega dE_f} \right)_{Q', \hbar\omega'} \times R [Q(\theta, \hbar\omega) - Q', (\hbar\omega - \hbar\omega')] dQ' d\hbar\omega'. \quad (6)$$

Figure 4 shows that both  $Q$  and  $\hbar\omega$  vary in a single time-of-flight scan. Thus the analysis of time-of-flight spectra is somewhat more complicated than "constant  $Q$ " spectra such as those obtained with triple-axis spectrometers. We proceeded as follows: First, a form for the dispersion relation (apart from an additive constant) was assumed over the restricted range of  $Q$  values in the time-of-flight spectrum. The width  $\hbar\Gamma(Q)$  was assumed constant. Then a folded least-squares fit was made to the data, treating the additive constant, the width  $\hbar\Gamma(Q)$ , and a normalization constant as varying fit parameters. This was done for each of the 14 time-of-flight spectra associated with an individual run and provided a first estimate of the dispersion relation. This estimate was then used in a second round of the folding-fitting procedure to obtain final values for the fitting parameters. Each time-of-flight spectrum thus yielded one point of the dispersion curve and a corresponding width  $\hbar\Gamma(Q)$ . We investigated the consequences of assuming that  $\hbar\Gamma(Q)$  was constant over the  $Q$  range included within a single spectrum and concluded that this assump-

tion had no significant influence on the results.

In Fig. 5 we show the best fit obtained for a typical time-of-flight spectrum using the Lorentzian cross section of Eq. (4). Note that the Boltzmann factor has completely damped out the annihilation peak at negative  $\hbar\omega$ . Nevertheless, the annihilation part of the cross section does have an influence at positive values of  $\hbar\omega$  because of its width. It should be noted that this effect is particularly important when the width  $\hbar\Gamma(Q)$  becomes comparable to the excitation energy  $\hbar\omega(Q)$ . In this case the Jacobian in (5) combines with the Boltzmann factor and the annihilation contribution from (4) to distort the observed spectrum. When this occurs, the position of maximum intensity is shifted so that it no longer corresponds to  $\hbar\omega(Q)$ . Thus at temperatures near  $T_{\lambda}$ , where the linewidth becomes significant, our dispersion curves are systematically shifted from those previously reported.

#### IV. EXPERIMENTAL RESULTS

##### A. Dispersion Curve

Our measurements were restricted to the wave-vector region near the roton minimum since we were particularly interested in the behavior of the roton parameters. Previous studies have shown how the dispersion curve at the saturated vapor pressure changes as the temperature approaches and finally exceeds  $T_{\lambda}$ .<sup>5</sup> There is also a single measurement showing how the dispersion curve at

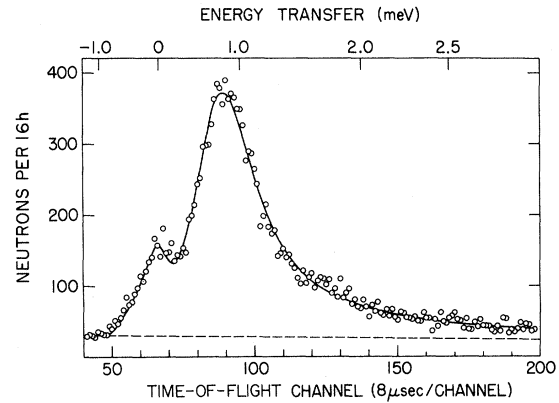


FIG. 5. Typical time-of-flight spectrum obtained at 2.11 °K at a scattering angle of 97°. The shoulder at zero energy transfer is produced by incoherent scattering from the Al sample cell. The dashed line corresponds to the background intensity and is slightly sloped because a tail of very slow scattered neutrons from the previous pulse is included in it. Drawn through the experimental points is the best fit of the Lorentzian cross section, [Eqs. (1) and (4)], with  $\hbar\omega(Q) = 0.83$  meV and  $\hbar\Gamma(Q) = 0.37$  meV, folded with the resolution function and transformed to a time-of-flight coordinate system. The weighted  $\chi^2$  for this fit is 1.14—for a damped harmonic-oscillator cross section the best fit yielded a  $\chi^2 = 2.16$ .

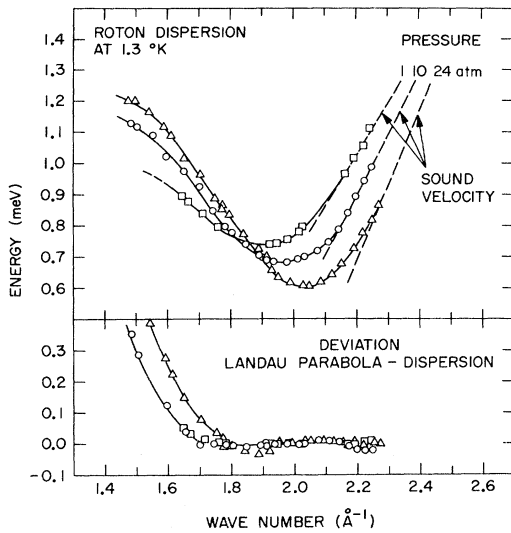


FIG. 6. Above: three dispersion curves in the region of the roton minimum at 1.3 °K and pressures of 1, 10, and 24 atm. Note that the slopes at higher  $Q$  correspond to the sound velocities, except at the highest pressure where the measurements do not extend far enough in  $Q$  to be definitive. Below: difference between the dispersion curve and best-fitting Landau parabola [Eq. (7)]. The parabola satisfactorily represents the excitation energies in the region about  $0.25 \text{ \AA}^{-1}$  to either side of  $Q_0$ . In both parts of the figure the smooth lines drawn through the points serve merely as an aid to the eye.

low temperatures is altered by pressure.<sup>6</sup> What we have undertaken here is a systematic investigation of the roton region of the dispersion curve over the entire pressure-temperature phase space of superfluid helium above 1.3 °K. In addition, we have made a few measurements in the normal-fluid region and in the hcp solid phase.

To present the essential results obtained from so large an amount of data in a reasonably condensed form we have used the conventional Landau parameters<sup>4</sup> to describe the roton region of the dispersion curve. Each of the dispersion curves measured at a specific temperature and pressure was therefore analyzed as described in Sec. III and then fitted to a parabola of the form

$$\hbar\omega(Q) = \Delta + \hbar^2(Q - Q_0)^2/2\mu. \quad (7)$$

In this expression  $\Delta$  represents the minimum energy,  $Q_0$  is the wave number at the minimum, and  $\mu$  is the effective mass.

In Fig. 6 we have shown three representative dispersion curves measured at 1.3 °K at pressures between 1 and 24 atm. As the pressure increases, the minimum energy  $\Delta$  decreases, the effective mass  $\mu$  is reduced, and the minimum wave number  $Q_0$  is pushed toward larger values. Away from  $Q_0$ , on the high- $Q$  side, the slopes of the dispersion

curves correspond to the sound velocities, except at the highest pressures where the measurements do not extend far enough out in  $Q$  to be definitive. However, Henshaw and Woods's<sup>6</sup> single high-pressure measurement at 25.3 atm covers a wide-enough  $Q$  range to indicate that the slope at this pressure does not quite reach the sound velocity. On the low- $Q$  side, there is a downward bending reflecting the transition to the intermediate region between phonons and rotons where the curves pass through a maximum. As an indication of how well the parabolic form of Eq. (7) fits the region near  $Q_0$ , we have plotted on the lower part of Fig. 6 the differences between the dispersion curves and the best fitting parabolas. It is evident that Eq. (7) is a statistically satisfactory representation of a region extending about  $0.25 \text{ \AA}^{-1}$  to either side of  $Q_0$  at all pressures. We see no indications of the asymmetry reported by Cowley and Woods<sup>5</sup> within the approximate range  $\pm 0.25 \text{ \AA}^{-1}$ .

Figure 7 shows the dispersion curves at 1 atm at various temperatures between 1.26 and 2.4 °K. Note that there is a change in the energy scales on the figure which obscures the fact that the minimum energy  $\Delta$  is reduced by more than a factor of 2 as the temperature increases. Since the lines also broaden with increasing temperature, the uncertainty in determining the excitation energy also increases. This is reflected in the larger statistical

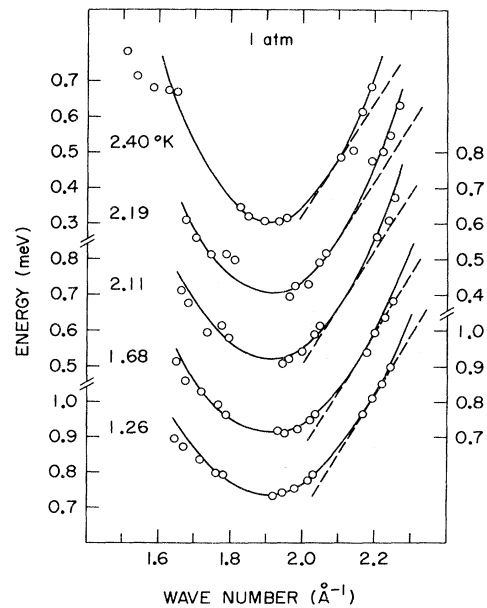


FIG. 7. Dispersion curves at 1 atm for various temperatures. The energy scales alternate from left to right. Note, in particular, the renormalization of the minimum energy as the temperature increases. The dashed lines have slopes corresponding to the sound velocity. The curves are the best fitting Landau parabolas.

TABLE I. Landau parameters  $\Delta$ ,  $Q_0$ , and  $\mu$  and linewidth  $\hbar\Gamma(Q_0)$ . With the units in the table the excitation energy is calculated from the expression  $E = \Delta + 0.515 (Q - Q_0)^2/\mu$ .

| Pressure (atm) | Temp. <sup>a</sup> (°K) | $\Delta$ (meV) | $Q_0$ ( $\text{\AA}^{-1}$ ) | $\mu$ ( $m_{He}$ ) | $\hbar\Gamma(Q_0)$ (meV) |
|----------------|-------------------------|----------------|-----------------------------|--------------------|--------------------------|
| 1.00           | 1.26                    | 0.736          | 1.902                       | 0.160              | <0.05                    |
| 1.00           | 1.45                    | 0.737          | 1.899                       | 0.165              | <0.05                    |
| 1.00           | 1.68                    | 0.711          | 1.911                       | 0.154              | <0.05                    |
| 1.00           | 2.11                    | 0.521          | 1.907                       | 0.137              | 0.23                     |
| 1.00           | 2.13                    | 0.488          | 1.917                       | 0.126              | 0.27                     |
| 1.00           | 2.15                    | 0.417          | 1.909                       | 0.117              | 0.30                     |
| 1.00           | 2.17                    | 0.397          | 1.915                       | 0.118              | 0.32                     |
| 1.00           | 2.18                    | 0.367          | 1.898                       | 0.092              | 0.32                     |
| 1.00           | 2.19                    | 0.403          | 1.910                       | 0.124              | 0.30                     |
| 1.00           | 2.20                    | 0.348          | 1.921                       | 0.11               | 0.36                     |
| 1.00           | 2.23                    | 0.361          | 1.898                       | 0.17               | 0.32                     |
| 1.00           | 2.25                    | 0.304          | 1.925                       | 0.11               | 0.37                     |
| 1.00           | 2.30                    | 0.265          | 1.927                       | 0.12               | 0.35                     |
| 1.00           | 2.40                    | 0.302          | 1.915                       | 0.11               | 0.38                     |
| 1.00           | 2.50                    | 0.254          | 1.912                       | 0.13               | 0.39                     |
| 1.00           | 4.37                    | 0.320          | 1.761                       | 0.23               | 0.6                      |
| 4.97           | 1.31                    | 0.706          | 1.940                       | 0.151              | <0.05                    |
| 5.02           | 1.46                    | 0.707          | 1.944                       | 0.148              | <0.05                    |
| 5.01           | 1.68                    | 0.686          | 1.947                       | 0.146              | 0.06                     |
| 4.99           | 1.82                    | 0.650          | 1.947                       | 0.142              | 0.10                     |
| 4.89           | 2.05                    | 0.483          | 1.950                       | 0.122              | 0.22                     |
| 5.04           | 2.17                    | 0.302          | 1.954                       | 0.11               | 0.33                     |
| 10.07          | 1.29                    | 0.680          | 1.962                       | 0.149              | <0.05                    |
| 9.91           | 1.47                    | 0.669          | 1.968                       | 0.140              | <0.05                    |
| 10.01          | 1.68                    | 0.650          | 1.973                       | 0.144              | 0.07                     |
| 10.14          | 1.81                    | 0.602          | 1.975                       | 0.131              | 0.13                     |
| 10.05          | 2.00                    | 0.427          | 1.982                       | 0.116              | 0.24                     |
| 10.03          | 2.10                    | 0.273          | 1.982                       | 0.12               | 0.31                     |
| 15.06          | 1.28                    | 0.660          | 1.998                       | 0.140              | <0.05                    |
| 14.97          | 1.46                    | 0.646          | 1.989                       | 0.141              | <0.05                    |
| 14.95          | 1.68                    | 0.618          | 1.999                       | 0.134              | 0.08                     |
| 15.07          | 1.82                    | 0.545          | 2.002                       | 0.129              | 0.14                     |
| 15.25          | 1.95                    | 0.352          | 2.006                       | 0.105              | 0.24                     |
| 15.05          | 2.05                    | 0.241          | 2.013                       | 0.12               | 0.30                     |
| 20.00          | 1.26                    | 0.631          | 2.015                       | 0.130              | <0.05                    |
| 20.20          | 1.47                    | 0.617          | 2.009                       | 0.138              | 0.06                     |
| 20.06          | 1.68                    | 0.547          | 2.017                       | 0.126              | 0.11                     |
| 20.10          | 1.81                    | 0.438          | 2.023                       | 0.106              | 0.19                     |
| 19.90          | 1.90                    | 0.273          | 2.028                       | 0.112              | 0.24                     |
| 20.18          | 1.99                    | 0.196          | 2.030                       | 0.11               | 0.25                     |
| 24.26          | 1.25                    | 0.610          | 2.028                       | 0.127              | <0.05                    |
| 24.35          | 1.46                    | 0.584          | 2.022                       | 0.123              | 0.06                     |
| 24.35          | 1.67                    | 0.493          | 2.022                       | 0.124              | 0.14                     |
| 24.15          | 1.82                    | 0.301          | 2.033                       | 0.104              | 0.22                     |
| 24.29          | 1.91                    | 0.166          | 2.003                       | 0.13               | 0.25                     |
| 24.50          | 4.37                    | 0.192          | 1.951                       | 0.15               | 0.5                      |

<sup>a</sup>Values of  $T_\lambda$  at different pressures can be found on Fig. 14.

scatter in the higher-temperature points. The dashed lines in Fig. 7 are drawn with slopes corresponding to the sound velocities. As we pointed out in connection with Fig. 6, the dispersion curves at larger- $Q$  values appear at low temperatures to have slopes characteristic of the sound velocities. At higher temperatures, however, there is a slight indication that the slopes may exceed the sound

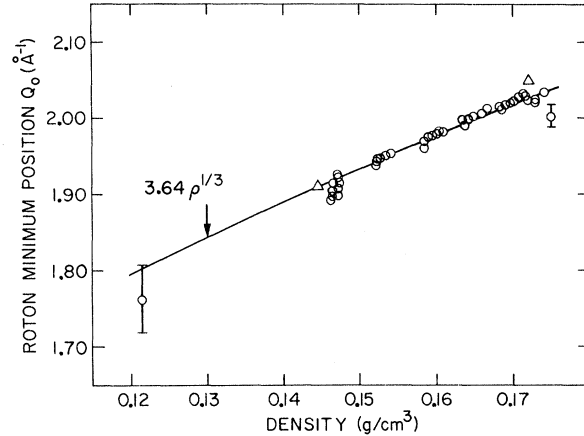


FIG. 8. The position of the roton minimum  $Q_0$  plotted against the density of the liquid. At all pressures and temperatures,  $Q_0$  is related to the density by the simple expression  $Q_0 = 3.64\rho^{1/3}$ , indicating that the number of nearest neighbors remains constant. The two triangles represent the 1.1 °K results of Henshaw and Woods (Ref. 3) at the saturated vapor pressure and at 25.3 atm. Error bars are shown where the statistical uncertainties exceed the size of the points.

velocity.

All of our results for the Landau parameters are collected in Table I and most of them are plotted in Figs. 8–10. Statistical uncertainties are not given in the table, but representative error bars can be found on the figures.

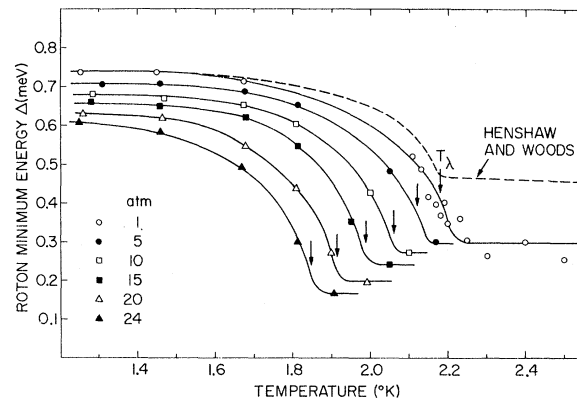


FIG. 9. The roton minimum energy  $\Delta$  plotted against the temperature for a series of pressures.  $T_\lambda$  temperatures are indicated by the arrows. At the lowest temperatures the uncertainties are within the size of the points. They increase to about twice the size of the points at the highest temperatures. At the lowest temperature, when the linewidth is negligible, our 1-atm results agree with those of Henshaw and Woods (Ref. 3) (dashed line). On approaching  $T_\lambda$ , the linewidth becomes significant and their values of  $\Delta$  lie above ours. This is believed to be an effect of the Boltzmann factor in Eq. (4). The lines are drawn through the data as a convenience and have no theoretical significance.

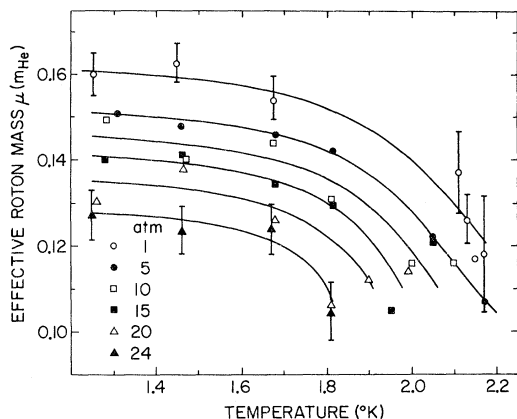


FIG. 10. The effective roton mass  $\mu$  in units of the  $\text{He}^4$  mass plotted against temperature for different pressures. The smooth lines drawn through the data are intended simply as an aid to the eye.

Figure 8 shows the position of the minimum,  $Q_0$ , plotted against the liquid density. Our data at all pressures and temperatures indicate that  $Q_0$  fits the universal curve  $Q_0 = A\rho^{1/3}$  with  $A = 3.64 \text{ cm g}^{-1/3} \text{ \AA}^{-1}$ .

Assuming that the minimum occurs at  $2\pi/a_{nn}$  (where  $a_{nn}$  is the average nearest-neighbor distance), this relation implies that the number of nearest neighbors in the superfluid is independent of both pressure and temperature. A simple cubic packing with six nearest neighbors would give  $A = 3.34$ , a bcc packing with eight nearest neighbors would give 3.65 and a dense fcc or hcp packing with 12 nearest neighbors,  $3.75 \text{ cm g}^{-1/3} \text{ \AA}^{-1}$ . We conclude that our results strongly support the view that the minimum occurs at  $2\pi/a_{nn}$  and that the average number of nearest neighbors remains almost constant and with a value close to that of a bcc lattice.

The minimum roton energy  $\Delta$  is plotted in Fig. 9. The curves are extended above  $T_\lambda$  as horizontal lines since measurements at  $4.37^\circ\text{K}$  (which appear in Table I but are not plotted on the figure) indicate that  $\Delta$  is almost independent of  $T$  in the normal fluid. At all temperatures  $\Delta$  is depressed by increasing pressure. We have found that this data can be equally well plotted as a single universal curve by replacing  $T$  by  $[T_\lambda(P) - T]$  (where  $P$  is the pressure) and  $\Delta$  by  $\Delta - \Delta_n$ . Here  $\Delta_n$  is the value of the minimum energy when  $T > T_\lambda$ . Henshaw and Woods's results<sup>3</sup> also appear as the dashed line on the figure. It is evident that their saturated-vapor-pressure data agree with our low-pressure data at low temperatures where the lines are narrow. At higher temperatures, however, where the linewidths become important, Henshaw and Wood's values are significantly larger than ours. Since the positions of maximum intensity in our observed spectra correspond at all tempera-

tures to their values of  $\Delta$ , the difference results from the way the data were analyzed. We have in effect removed the distortions due to the Boltzmann factor in Eq. (4) before fitting to determine  $\Delta$ .

In Fig. 10 we have plotted the temperature dependence of the effective roton mass  $\mu$  at various pressures. Qualitatively,  $\mu$  behaves in the same way as  $\Delta$ , decreasing with increasing pressure and temperature. Henshaw and Woods's value<sup>3</sup> of 0.16  $m_{\text{He}}$  at  $1.1^\circ\text{K}$  and the saturated vapor pressure is consistent with our findings.

It is also possible to determine from the normalization constant  $C(Q)$  in Eq. (4), the single-excitation contribution to the scattering function, i.e.,  $S_1(Q) = \int S_1(Q, \hbar\omega) d(\hbar\omega)$ . This function is shown in Fig. 11 for three different pressures at  $1.3^\circ\text{K}$  (the corresponding dispersion curves appear in Fig. 6).  $S_1(Q)$  represents only the single-excitation contribution to  $S(Q)$ ; there is also a large "multiphonon" contribution which is known from the work of Cowley and Woods.<sup>5</sup> This does not appear in our data because of the low neutron energy used.

Larsson, Dahlborg, and Jovic<sup>15</sup> have remarked on the similarity of the inelastic scattering spectra of liquid and polycrystalline solid aluminum. The same is also true of helium. Figure 12 shows a time-of-flight spectrum obtained in the polycrystalline solid hcp phase of helium together with spectra taken in the liquid phase at 24 atm at temperatures of 1.25 and 1.82 $^\circ\text{K}$ . The inelastic scattering occurs over about the same range of energies in the polycrystalline solid and liquid, but the solid spec-

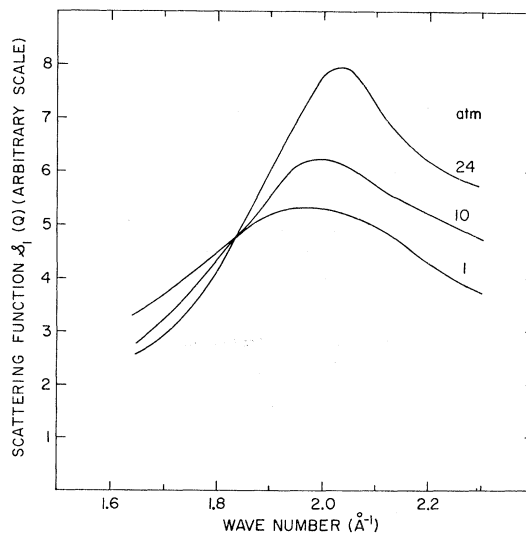


FIG. 11. The single excitation scattering function  $S_1(Q) = \int S_1(Q, \hbar\omega) d(\hbar\omega)$  for three different pressures at  $1.3^\circ\text{K}$ . (See Fig. 6 for the corresponding dispersion curves.) At higher pressure the peak becomes higher and narrower, probably an indication of increasing order in the liquid.

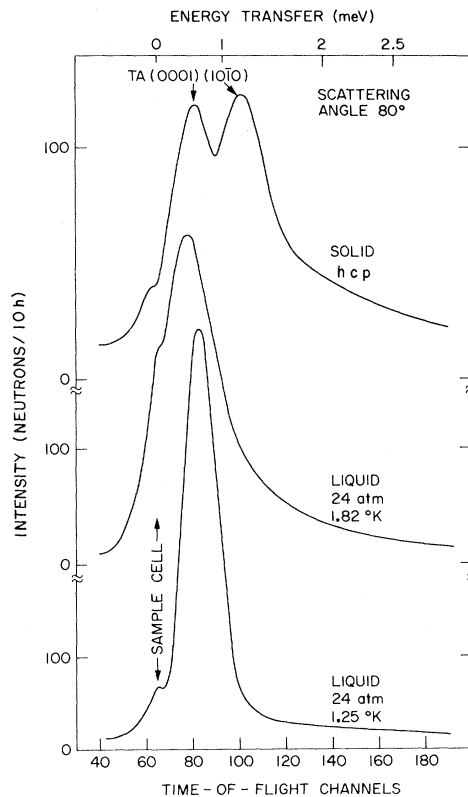


FIG. 12. The time-of-flight spectra of polycrystalline solid helium (upper curve) and of the liquid (lower curves) are similar in certain respects. Large contributions to the scattering from the solid can be identified with zone boundary phonons and give rise to the observed structure. Note, however, that the over-all energy range of the scattering is about the same especially when the rotons have significant linewidths (middle curve).

trum shows structure which is not present in the liquid. We have found that we can reproduce qualitatively the polycrystalline spectrum in Fig. 12 from the measured phonon dispersion in hcp helium<sup>16</sup> simply by a numerical integration over all phonons in  $q$  space which contribute to the intensity from a polycrystalline sample. The peaks in the solid spectrum occur at energies corresponding to peaks in the phonon density of states and result from the flat parts of the dispersion curves near the zone boundaries. Thus the two peaks appearing in the upper spectrum in Fig. 12 are associated with transverse acoustical modes near (0001) and (1010), respectively.

If we use the "center of gravity" of the solid spectra observed at different scattering angles to define an "average dispersion curve" for the polycrystalline solid, the curve we obtain shows a marked resemblance to the dispersion curve seen in superfluid helium, including the dip characteristic of the roton region. This is also evident from the calculations of polycrystalline neutron cross

sections made by deWette and Rahman.<sup>17</sup> One hesitates to push the analogy between the polycrystalline solid and liquid phases of helium too far; nevertheless, it is interesting that the counterpart of the scattering which appears as the roton peak in superfluid helium is predominantly zone-boundary phonon scattering in the polycrystalline solid.

### B. Linewidths

At temperatures below 1.4 °K the widths of almost all of the observed time-of-flight spectra are resolution limited. The bottom spectrum of Fig. 12 is a typical example. When these spectra were analyzed, the resulting unfolded widths near the minimum position  $Q_0$  and on the low- $Q$  side of  $Q_0$  had small positive values less than 0.05 meV, i.e., less than one-quarter of the instrumental resolution width. Of course, widths this small are not in themselves statistically significant, but by their consistency they assure us that our resolution-function calculations and unfolding procedures are reliable.

On the high- $Q$  side of  $Q_0$ , except possibly at the highest pressures, we found significant linewidths even at the lowest temperatures. This is shown in Fig. 13 for three pressures at 1.3 °K (the three corresponding dispersion curves appear in Fig. 6). At higher temperatures the effect is less pronounced since some line broadening is observed for all  $Q$  values. It is striking that this sudden increase in linewidth occurs at approximately the same values of  $Q$  at which the slopes of the dis-

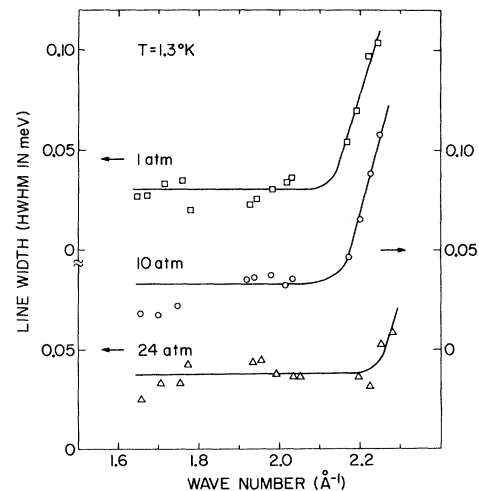


FIG. 13. Linewidths HWHM,  $\hbar\Gamma(Q)$ , at 1.3 °K for various pressures; width scales alternate from left to right. Note the sudden increase in the widths at values of  $Q$  at which the slopes of the dispersion curves equal the sound velocities (see Fig. 6). At smaller values of  $Q$  the lines are too narrow to be resolved. The smooth lines drawn through the points have no theoretical significance.

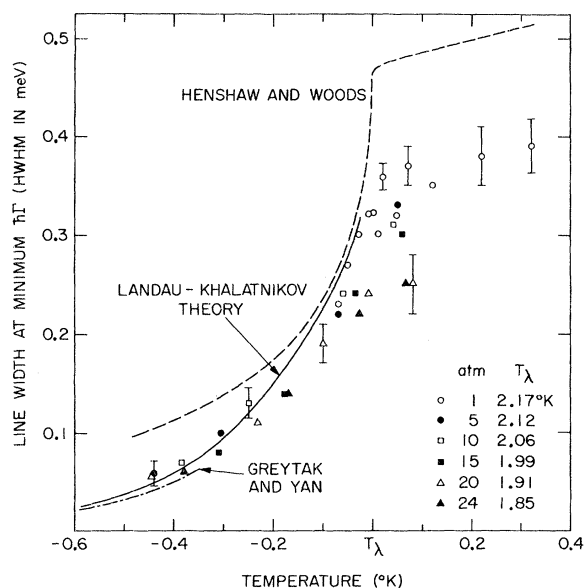


FIG. 14. Linewidths HWHM at the position of the roton minimum plotted against  $T - T_\lambda(P)$ . Values of  $T_\lambda$  at the different pressures taken from Ref. 21 are listed in the lower right corner. Reasons for the differences between our results and those of Henshaw and Woods (Ref. 3) are discussed in Sec. IV B. The increase in linewidth as  $T$  approaches  $T_\lambda$  is in quantitative agreement with the calculation of Landau and Khalatnikov (Ref. 20). Greytak and Yan's (Ref. 23) results are represented by the dash-dotted curves.

persion curves become equal to the sound velocities. As Pitaevskii suggested, from this point on the energy and momentum conservation laws allow a roton to decay into another roton by either emitting or absorbing a phonon.<sup>18</sup> There is little reason to doubt that the sudden increase in linewidth is connected with the appearance of this scattering process.<sup>19</sup>

On a theoretical basis, the line broadening associated with this roton-phonon interaction is expected to increase as  $(Q - Q_c)^3$ , where  $Q_c$  is the wave number at which the slope of the dispersion curve equals the sound velocity. Because the linewidths are small and  $Q_c$  is difficult to determine with any accuracy, we do not feel that our present data can be used for a quantitative comparison with theory. Nonetheless, the steep increase we observe is not inconsistent with the proposed  $(Q - Q_c)^3$  dependence.

Typically at temperatures about  $0.5^\circ\text{K}$  below  $T_\lambda$ , the linewidth  $\hbar\Gamma(Q)$  becomes large enough to be resolved over the entire  $Q$  range. We have tabulated in Table I the values of  $\hbar\Gamma(Q)$  obtained at the roton minimum position. The same data are also plotted in Fig. 14 as a single universal curve using as the abscissa  $T - T_\lambda(P)$ , where  $P$  is the pressure. It is clear from Fig. 14 that below  $T_\lambda$  the width is a func-

tion of  $T - T_\lambda(P)$  independent of pressure. Above  $T_\lambda$ , the width is almost independent of temperature but there is some indication of a decrease with increasing pressure.

The smoothed results of Henshaw and Woods<sup>3</sup> appear as the dashed curve on Fig. 14. They are consistently above ours. Again the difference can be traced to the way in which the data were analyzed. We are reporting unfolded widths. Therefore at low temperatures, where the lines are narrow, instrumental resolution effects alone account for the difference. At higher temperatures, however, another factor comes into play. We assumed the double-peaked cross section of Eq. (4) which contains terms representing both annihilation and creation of excitations. The annihilation peak is suppressed by the Boltzmann factor when it is narrow and the excitation energy is reasonably large. But near  $T_\lambda$  the excitation energy renormalizes and the lines are wide enough to overlap. As a result both the annihilation and creation peaks contribute to the width of the observed line, the quantity reported by Henshaw and Woods. What is plotted in Fig. 14, however, is not the width of the observed lines but the spectral width of the excitations—hence the difference.

Landau and Khalatnikov<sup>20</sup> have developed a theory for roton linewidths which applies to the present measurements. They assumed roton-roton scattering to be the dominant process. Estimating the linewidth in terms of  $\eta_r$ , the viscosity of the normal fluid, they obtained the following expression:

$$\hbar\Gamma(Q) = \frac{\hbar^3 Q_0^2 N_r}{30 \mu \eta_r} = \frac{\hbar^2 Q_0^4}{15 \eta_r} \left( \frac{kT}{(2\pi)^3 \mu} \right)^{1/2} e^{-\Delta/kT}. \quad (8)$$

$N_r$ , the number of rotons per unit volume, has been approximated in the second equation by the value obtained assuming the roton dispersion curve to be parabolic.<sup>21</sup> To calculate  $\hbar\Gamma(Q)$  from Eq. (8) we have used the viscosity measurements of Woods and Hollis Hallett<sup>22</sup> together with our own values of the Landau parameters at 1 atm. As is evident in Fig. 14, the agreement with our measured linewidths is very good.

Greytak and Yan<sup>23</sup> have measured roton linewidths in the temperature range  $1.35$ – $1.83^\circ\text{K}$  using Raman scattering from two-roton processes. Their results appear in Fig. 14 as the dash-dotted curve. It is gratifying that their data are in reasonable agreement with the Landau-Khalatnikov curve calculated from our measurements.

The linewidth  $\hbar\Gamma(Q)$  has its minimum value at the roton minimum  $Q_0$ . To either side of the minimum  $\hbar\Gamma(Q)$  increases almost parabolically. It is illuminating to plot the reduced linewidth  $\hbar\Gamma(Q)/\hbar\omega(Q)$  (i. e., the linewidth divided by the excitation energy) against the wave number  $Q$  as we have done in Fig. 15. Here we show the 10-atm results (which are

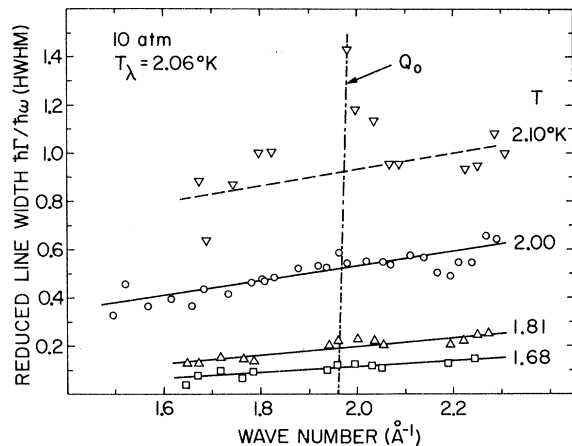


FIG. 15. Reduced linewidths [i.e., the linewidth  $\hbar\Gamma(Q)$  divided by the excitation energy  $\hbar\omega(Q)$ ] plotted against the wave number  $Q$  for different temperatures at 10 atm. The dash-dotted line indicates the position of the roton minimum  $Q_0$ . Note that  $\hbar\Gamma(Q)/\hbar\omega(Q)$  varies smoothly with  $Q$  below  $T_\lambda$ , but above  $T_\lambda$  an anomaly appears to develop at  $Q_0$ . The straight lines are drawn through the data as an aid to the eye.

typical of all our measurements) at various temperatures between 1.7 and 2.1 °K. The dash-dotted line denotes the position of  $Q_0$ . Below  $T_\lambda$  there is a smooth and regular behavior, but above  $T_\lambda$  there are indications at all pressures of a maximum developing at  $Q_0$ . Unfortunately the scatter in the data is large, particularly above  $T_\lambda$ . This is unavoidable. It occurs because the uncertainties of the reduced widths involve the combined uncertainties of  $\hbar\Gamma(Q)$  and  $\hbar\omega(Q)$ .

At all pressures the same trend toward a small but steady increase in reduced linewidth with  $Q$  is observed. We found that by using the temperature difference  $T - T_\lambda(P)$  as a variable all of the reduced linewidth data below  $T_\lambda$  can be represented by the set of universal curves shown in Fig. 16. By using this figure and the Landau parameters listed in Table I the reader can obtain the unfolded linewidths at all temperatures, pressures, and wave numbers to an accuracy of about 15%.

We know of no theoretical model which can explain the simple behavior of the reduced linewidths displayed in Figs. 15 and 16. Nevertheless, it appears to hold over a considerable range of  $Q$ . In fact there are indications that the smooth behavior may even extend to smaller- $Q$  values than those covered by our measurements. If we make a linear extrapolation of the reduced linewidths of Fig. 16 to the phonon region we obtain values in rough agreement with those observed by Cowley and Woods<sup>5</sup> at the saturated vapor pressure. For example, at 2.1 °K and  $Q = 0.6 \text{\AA}^{-1}$ , Cowley and Woods found the full width at half-maximum (FWHM) of the phonon line to be about

4.5 °K at a phonon energy of 10.6 °K. Using their observed line at 1.1 °K to roughly unfold the instrumental width, we obtain for  $\hbar\Gamma(Q)/\hbar\omega(Q)$  the value 0.20. A linear extrapolation from Fig. 16 yields 0.17. Possibly the agreement is fortuitous, but it is clear that the point bears further investigation.

## V. DISCUSSION

### A. Thermodynamic Relationships

One of the unique properties of superfluid helium is that all of the internal energy is associated with collective excitations. Therefore the free energy of the liquid and the thermodynamic properties calculated from it are fully determined by the excitation spectrum. Below roughly 0.6 °K, only the phonon states are populated and accordingly in this temperature region they dominate the thermodynamics. In the region of our measurements, above 1.3 °K, the roton states are also occupied. Because large wave vectors are associated with rotons, the number of roton states is much larger than the number of phonon states. Consequently, at higher temperatures the rotons tend to dominate most of the thermodynamic properties.

Bendt, Cowan, and Yarnell<sup>24</sup> have shown how neutron-scattering data can be utilized to calculate the thermodynamic properties of liquid helium. Using the measured saturated-vapor-pressure dispersion curves they calculated values for the entropy, specific heat, normal-fluid density and sound velocity in good agreement with those obtained by direct measurements. Later, Cohen<sup>14</sup> subjected the assumptions underlying these calculations to careful scru-

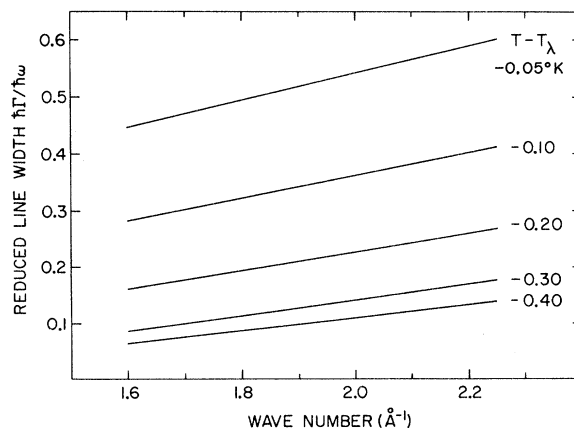


FIG. 16. The lines represent values of the reduced linewidth  $\hbar\Gamma(Q)/\hbar\omega(Q)$  averaged over all pressures for the same temperature difference  $T - T_\lambda(P)$  plotted against wave number  $Q$ . Using the Landau parameters of Table I and the lower part of Fig. 6 to calculate  $\hbar\omega(Q)$  together with the  $T_\lambda$  values listed on Fig. 14 the reader can determine the unfolded linewidth  $\hbar\Gamma(Q)$  at any pressure, temperature, and wave number to an accuracy of about  $\pm 15\%$ .

tiny and concluded that the simple connections between the thermodynamic properties and neutron-scattering data derived by Bendt *et al.* hold only if the interactions between excitations are weak. Cohen suggested that the ratio of the linewidth  $\hbar\Gamma(Q)$  to the line shift [i. e., the *renormalization* of the excitation energy  $\hbar\omega(Q)$ ] be used as a criterion to judge the strength of the interaction. A weak interaction is, in Cohen's terms, one in which the linewidth is small compared to the excitation energy shift. Since the roton linewidth is comparable to the line shift, Cohen argued that the interactions between rotons are not weak and therefore the agreement found by Bendt *et al.* was of questionable significance.

Our measurements offer additional opportunities to test the validity of the relationships formulated by Bendt *et al.* between the thermodynamic properties of the liquid and the neutron-scattering data. We have calculated both the entropy  $S$  and the superfluid density  $\rho_s$  following basically the same procedure but with a slight modification to take into account the linewidth of the dispersion curve. When the linewidth is neglected, the entropy is related to the measured dispersion curve  $\hbar\omega(Q)$  by the expression<sup>24</sup>

$$S = \frac{k_B}{2\pi^2\rho} \int_0^\infty \left( \frac{\hbar\omega(Q)\beta}{e^{\hbar\omega(Q)\beta} - 1} - \ln(1 - e^{-\hbar\omega(Q)\beta}) \right) Q^2 dQ. \quad (9)$$

For the superfluid density there is a corresponding relationship

$$\rho_s = \rho - \frac{\hbar^2\beta}{6\pi^2} \int_0^\infty \frac{e^{\hbar\omega(Q)\beta}}{[e^{\hbar\omega(Q)\beta} - 1]^2} Q^4 dQ. \quad (10)$$

To include the linewidth in the above expressions,  $\hbar\omega(Q)$  is replaced by  $(\hbar/\pi)\Gamma(Q)/\{\hbar^2\Gamma^2(Q) + [\hbar\omega - \hbar\omega(Q)]^2\}$  and an additional integration over  $\hbar\omega$  is performed at each  $Q$ . The sound velocity was used to define the slope of the phonon part of the dispersion curve and the roton and phonon regions were connected by a suitable parabola.<sup>25</sup> Calculations of the entropy using Eq. (9) are shown in Fig. 17 together with the measurements of van den Meijdenberg, Taconis, and de Bruyn Ouboter.<sup>26</sup> The agreement at low temperature is excellent. At higher temperatures, however, when the linewidth becomes important, the calculations give larger values for  $S$  than those measured directly. In Fig. 17 this is only evident at the higher pressures, but it also occurs at lower pressures at temperatures above 1.7 °K—the highest temperature included in the figure.

The relative superfluid density  $\rho_s/\rho$ , calculated from Eq. (10), is plotted in Fig. 18 for comparison with the measurements of Clow and Reppy.<sup>27</sup> As before, we find that by using a  $T_\lambda(P) - T$  scale we can plot the data obtained at all pressures on a single universal curve. We therefore conclude that

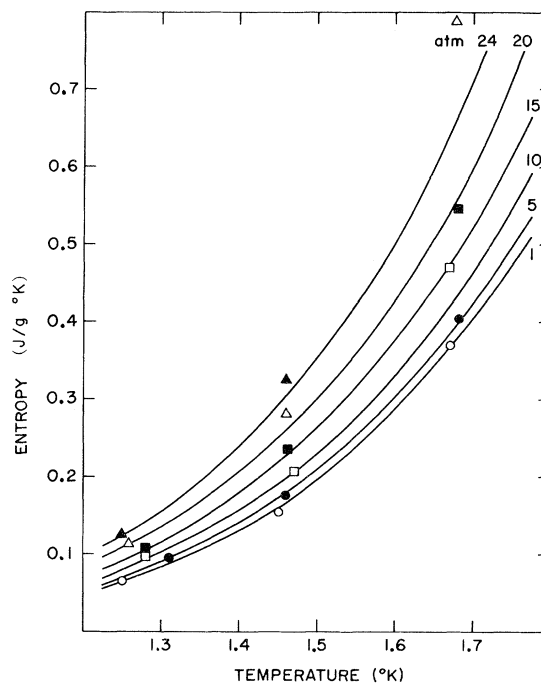


FIG. 17. The entropy as calculated from Eq. (9) using the measured values of the roton parameters and a linear phonon dispersion curve with slope equal to the sound velocity. Note that the agreement at low temperatures (where the linewidths are small) is very good but that the agreement becomes progressively poorer at higher temperatures as the lines broaden. The smooth lines represent the measurements of Ref. 26.

$\rho_s/\rho$  depends only on  $T_\lambda(P) - T$  regardless of pressure. Once again the calculations are in excellent agreement with direct measurements provided the linewidth is small compared to the excitation energy.

This considerable body of evidence influences us to believe that there is a simple relationship between the neutron data and the thermodynamic properties when the linewidth is small compared to the excitation energy. Cohen's criterion relating the linewidth to the *shift* in the excitation energy appears to us to be more restrictive than the experimental facts warrant.

For calculations of the thermodynamic properties of superfluid helium it is often convenient to express the free energy as a sum of two terms, one coming from the linear phonon region of the dispersion curve and the other from the parabolic roton region. For computations, it is necessary to have values for the density derivatives of the Landau parameters. Listed below are the values of these derivatives as determined from the data in Table I at 1.3 °K and extrapolated to the saturated vapor pressure:

$$\frac{\rho}{\Delta} \frac{\partial \Delta}{\partial \rho} = -0.94 \pm 0.05,$$

$$\frac{\rho}{Q_0} \frac{\partial Q_0}{\partial \rho} = 0.37 \pm 0.02,$$

$$\frac{\rho}{\mu} \frac{\partial \mu}{\partial \rho} = -1.1 \pm 0.1.$$

The first of these derivatives and the combination

$$\frac{1}{2} \frac{\rho}{\mu} \frac{\partial \mu}{\partial \rho} + 2 \frac{\rho}{Q_0} \frac{\partial Q_0}{\partial \rho} + \frac{\rho}{\Delta} \frac{\partial \Delta}{\partial \rho}$$

can also be evaluated by combining the measured values of the thermal expansion coefficient and the entropy. Harris-Lowe and Smee<sup>28</sup> have made the most recent attempt to do this and have also undertaken to reanalyze the earlier experiments which differed among themselves far beyond the limits of the statistical errors. Our results, which were obtained from direct measurements, are not in good agreement with those quoted by Harris-Lowe and Smee. In view of this we are tempted to question the reliability of the thermodynamic assumptions underlying their indirect approach.

### B. Roton Line Shape

It is interesting to see how the line spectra representing roton creation and annihilation renormalize, broaden, and finally coalesce into a single peak as the temperature of the liquid rises above  $T_\lambda$ . Examples of the line shapes are shown in Fig.

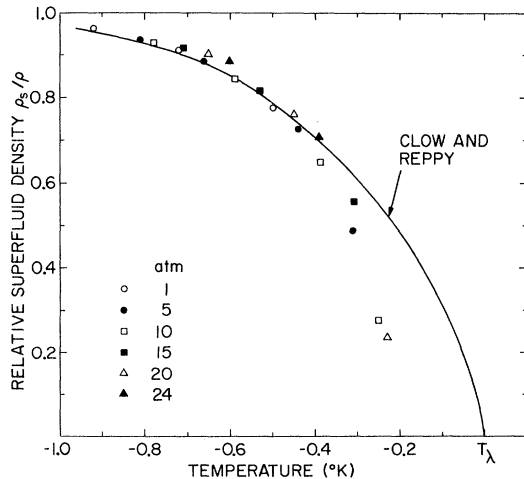


FIG. 18. The relative superfluid density as calculated from Eq. (10) using the measured values of the roton parameters and a linear phonon dispersion curve with slope equal to the sound velocity. The results are in good agreement with direct measurements at low temperatures where the linewidths are small. At higher temperatures the lines broaden and the agreement is poor.

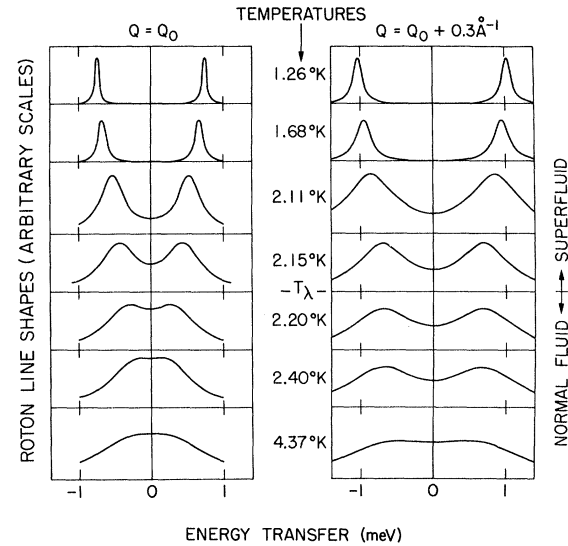


FIG. 19. The unfolded line shapes with the distorting effects of the Boltzmann factor removed. At  $Q=Q_0$  the annihilation and creation peaks merge slightly above  $T_\lambda$  while at  $Q=Q_0+0.3 \text{ \AA}^{-1}$  they retain their separate identities at a noticeably higher temperature.

19 for  $Q=Q_0$  and  $Q=Q_0+0.3 \text{ \AA}^{-1}$ . Note particularly that at  $Q=Q_0$  the annihilation and creation peaks have almost completely merged at  $T=T_\lambda$ , while at  $Q=Q_0+0.3 \text{ \AA}^{-1}$  they retain their separate identities above  $T_\lambda$ .

This behavior (which can also be deduced from Fig. 15) is remarkably similar to that observed for spin-wave spectra near the ordering temperature in magnetic systems.<sup>29,30</sup> The analogy is not surprising. Spin-wave renormalization is governed by the decrease in the magnetic-order parameter and spin-wave lifetimes are determined by magnon-magnon interactions. In superfluid helium the renormalization of roton energies is related by the superfluid density<sup>31</sup> to the order parameter of the superfluid, and roton lifetimes are determined by roton-roton interactions. Further, it is well established that long wavelength spin waves completely renormalize at the transition temperature  $T_c$  while the shorter wavelength modes persist above  $T_c$ , propagating within the short-range-ordered spin clusters. Thus rotons at  $Q_0$  behave very much like long-wavelength spin waves while rotons with wave numbers different from  $Q_0$  behave like shorter-wavelength spin waves and continue to propagate as discrete excitations above  $T_\lambda$ . It is appealing to interpret this as an indication that the liquid retains vestiges of the translational symmetry of the solid and that  $Q_0$  plays, in some sense, the role of a reciprocal lattice vector.

To us it is striking that the elementary excitations in such widely disparate critical systems as

magnets and superfluid helium are influenced by the change in the order parameter in such a similar way.

## VI. SUMMARY

We have performed a series of neutron-scattering studies designed to give a complete description of the properties of the roton excitations in the superfluid region above 1.3°K. The most important results are as follows: (i) The energy dependence of the roton line shapes is well approximated by the Lorentzian form suggested by Cohen.<sup>14</sup> (ii) The roton region of the dispersion curve is parabolic within a range of approximately  $0.25 \text{ \AA}^{-1}$  to either side of  $Q_0$ . (iii) On the high- $Q$  side of  $Q_0$ , except possibly at the highest pressures, the slope of the dispersion curve corresponds to the sound velocity. (iv) The Landau parameters  $\Delta$  and  $\mu$  decrease with increasing temperature and pressure.  $Q_0$  varies as the cube root of the liquid density, indicating that the average number of nearest neighbors remains at a constant value close to 8 over the entire temperature and pressure range. (v) At 1.3°K, the lowest temperature at which measurements were made, line broadening occurs on the high- $Q$  side of  $Q_0$  from the point at which the slope of the dispersion curve corresponds to the sound velocity. There are indications that this is due to roton-

phonon interactions. (vi) Line broadening is observed for all values of  $Q$  for  $T > T_\lambda - 0.4^\circ\text{K}$ . This broadening is well explained as a result of roton-roton interactions. (vii) The reduced linewidth (the linewidth divided by the excitation energy) is almost independent of  $Q$  for  $T < T_\lambda$ . (viii) The entropy and superfluid density calculated from the measured dispersion curve (taking the linewidth into account) agree with direct measurements at low temperatures where the linewidths are small. At higher temperatures, where the lines are wide, the thermodynamic relationships appear to break down. (ix) The density derivatives of the Landau parameters at 1.3°K and the saturated vapor pressure obtained from our direct measurements are not in good agreement with those obtained indirectly from analysis of the thermal expansion coefficient. (x) The roton line shapes both above and below  $T_\lambda$  are very similar to spin-wave line shapes in the neighborhood of the magnetic-ordering temperature.

## ACKNOWLEDGMENTS

We wish to thank Dr. Victor S. Emery and Dr. Martin Blume for many helpful discussions. We also wish to express our appreciation to Dr. Klaus Kehr for sharing with us his extensive knowledge of the theory of roton interactions and to Dr. Robert Nathans for his support and encouragement.

<sup>†</sup>Research supported by the United States Atomic Energy Commission.

\*Guest scientist, Brookhaven National Laboratory, Upton, N. Y.

<sup>1</sup>H. Palevsky, K. Otnes, and K. E. Larsson, *Phys. Rev.* **112**, 11 (1958).

<sup>2</sup>J. L. Yarnell, G. P. Arnold, P. J. Bendt, and E. C. Kerr, *Phys. Rev.* **113**, 1379 (1959); K. E. Larsson and K. Otnes, *Arkiv. Fysik* **15**, 49 (1959).

<sup>3</sup>D. G. Henshaw and A. D. B. Woods, *Phys. Rev.* **121**, 1266 (1961).

<sup>4</sup>L. D. Landau, *J. Phys. USSR* **11**, 91 (1947).

<sup>5</sup>R. A. Cowley and A. D. B. Woods, *Can. J. Phys.* **49**, 177 (1971).

<sup>6</sup>D. G. Henshaw and A. D. B. Woods, *Proceedings of the Seventh International Conference on Low Temperature Physics*, edited by G. M. Graham and A. C. Hollis Hallett (University of Toronto Press, Toronto, 1961), p. 539.

<sup>7</sup>K. Otnes and H. Palevsky, *Inelastic Scattering of Neutrons in Solids and Liquids* (IAEA, Vienna, 1963), Vol. I, p. 95.

<sup>8</sup>O. W. Dietrich, *Nucl. Instr. Methods* **61**, 296 (1968).

<sup>9</sup>M. J. Cooper and R. Nathans, *Acta Cryst.* **23**, 357 (1967).

<sup>10</sup>M. Nielsen and H. Bjerrum Møller, *Acta. Cryst.* **A25**, 547 (1969).

<sup>11</sup>S. Komura and M. J. Cooper, *Japan J. Appl. Phys.* **9**, 866 (1970).

<sup>12</sup>A. Tucciarone, H. Y. Lau, L. M. Corliss, A. Delapalme, and J. M. Hastings (unpublished); B. Dorner (unpublished).

<sup>13</sup>W. Marshall and S. W. Lovesey, *Theory of Thermal Neutron Scattering* (Oxford U. P., Cambridge, 1971).

<sup>14</sup>M. Cohen, *Phys. Rev.* **118**, 27 (1960).

<sup>15</sup>K. E. Larsson, U. Dahlborg, and D. Jovic, *Inelastic Scattering of Neutrons* (IAEA, Vienna, 1965), Vol. II, p. 117.

<sup>16</sup>V. J. Minkiewicz, T. A. Kitchens, F. P. Lipschultz, R. Nathans, and G. Shirane, *Phys. Rev.* **174**, 267 (1968).

<sup>17</sup>F. W. de Wette and A. Rahman, *Phys. Rev.* **176**, 784 (1968).

<sup>18</sup>L. P. Pitaevskii, *Zh. Eksperim. i Teor. Fiz.* **36**, 1168 (1959) [*Sov. Phys. JETP* **9**, 830 (1959)].

<sup>19</sup>We wish to thank Dr. K. Kehr for bringing this decay mechanism to our attention.

<sup>20</sup>L. D. Landau and I. M. Khalatnikov, *Zh. Eksperim. i Teor. Fiz.* **19**, 637 (1949).

<sup>21</sup>J. Wilks, *The Properties of Liquid and Solid Helium* (Oxford U. P., Oxford, 1967), p. 158.

<sup>22</sup>A. D. B. Woods and A. C. Hollis Hallett, *Can. J. Phys.* **41**, 596 (1963).

<sup>23</sup>T. J. Greytak and J. Yan, in *Proceedings of the Twelfth International Conference on Low Temperature Physics, Kyoto, 1970* (Academic of Japan, Tokyo, 1971).

<sup>24</sup>P. J. Bendt, R. D. Cowan, and J. L. Yarnell, *Phys. Rev.* **113**, 1386 (1959).

<sup>25</sup>The choice of the connecting parabola has very little effect on the final results since the  $Q$  region covered by our measurements contributes 98% of  $\rho_s$  and 80% of  $S$ . About 19% of  $S$  comes from the linear phonon region. Hence in neither case does the connecting parabola contribute more than about 2% to the result.

<sup>26</sup>C. J. N. van den Meijdenberg, K. W. Taconis, and R. de Bruyn Ouboter, *Physica* **27**, 197 (1961).

<sup>27</sup>J. R. Clow and J. D. Reppy, *Phys. Rev. Letters* **16**, 887 (1966).

<sup>28</sup>R. F. Harris-Lowe and K. A. Smee, *Phys. Rev. A* **2**, 158 (1970).

<sup>29</sup>M. F. Collins, V. J. Minkiewicz, R. Nathans, L.

Passell, and G. Shirane, *Phys. Rev.* **179**, 417 (1969).

<sup>30</sup>A. Tucciarone, L. M. Corliss, and J. M. Hastings, *J. Appl. Phys.* **42**, 1378 (1971).

<sup>31</sup>In the two-fluid model of superfluid helium the superfluid density is identified with the square of the order parameter (see for example, Ref. 21).

## Induced Compton Scattering and Nonlinear Propagation in Laser-Created Plasmas

M. Decroisette, J. Peyraud, and G. Piar

*Commissariat à l'Energie Atomique, Centre d'Etudes de Limeil,  
94-Villeneuve-Saint-George, France*

(Received 2 April 1971)

We have obtained some evidence of the induced scattering of an electromagnetic wave by Compton collisions, and of its nonlinear propagation in a plasma. The interpretation of the modified spectral profile of the interacting radiation is compatible with plasma parameters.

### I. INTRODUCTION

In 1933, Kapitza and Dirac suggested that electrons might be scattered by stationary light waves such as by using a diffraction grating.<sup>1</sup> We present this experiment in another form, without standing waves and where energy exchanges are possible. Let us focus a laser beam, i. e., a high radiative-energy flux, on a plasma by means of a lens. Besides ordinary Compton collisions, in which a photon is absorbed and reemitted spontaneously with a frequency shift in some given direction, the stimulated Compton effect must be taken into account. In fact, some scattered photons may belong to the incoming light in direction and in energy, because of the solid angle  $\Omega$  and the spectral linewidth  $\Delta\nu$  of the incident beam (Fig. 1). According to the quantum theory of radiation, they will be stimulated by the incoming photons and thus the scattering observed in the direction of the laser beam will be enhanced.

In our experiment, where the plasma is highly inhomogeneous and reflecting, for the incoming

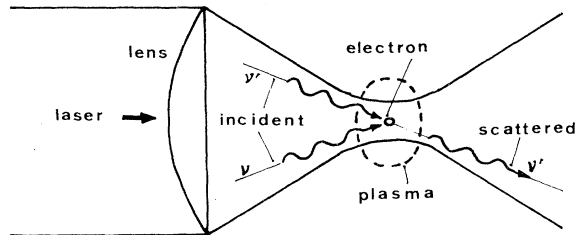


FIG. 1. Schematic diagram of stimulated Compton scattering.

laser light, the photon distribution can be considered nearly isotropic. Then it is possible to calculate the transfer of energy from photons to electrons, and the mean shift of the spectral profile towards the lower frequencies.

In the present paper, Sec. II is devoted to a theoretical investigation of stimulated Compton scattering effects in a plasma, Sec. III to the experimental setup, and Sec. IV to the interpretation of the experimental results.

### II. THEORETICAL CONSIDERATIONS

It has been shown that the Compton electron-photon interaction can be described in a kinetic theory by a Boltzman-like interaction operator (Refs. 2 and 3). The only difference from the classical Boltzmann operator is due to the boson nature of photons which introduces induced terms.

Let us note  $\vec{\nu} = \Omega\hat{x}$ , the vector frequency of a photon and  $N(\vec{\nu})$ , the photon distribution in frequency space. [If we deal with polarized photons we have to introduce the two functions  $N^i(\vec{\nu})$ ,  $i=1, 2$  according to the polarization.] The propagation equation, taking into account Compton effects, is

$$\left(\frac{\partial}{\partial t} + c\vec{\Omega} \frac{\partial}{\partial \vec{x}}\right) N^i(\nu) = c \int \sigma \{ [N^i(\nu') + c^3 N^i(\nu) N^i(\nu')] f(p') - [N^i(\nu) + c^3 N^i(\nu') N^i(\nu)] f(p') \} d\Omega' d\vec{p}, \quad (1)$$

where  $f(\vec{p})$  is the electron distribution function.

For unpolarized photons  $N^1(\vec{\nu}) = N^2(\vec{\nu}) = \frac{1}{2}N(\vec{\nu})$ . The equation for the total density  $N(\vec{\nu})$  is the same as Eq. (1) except for the replacement of  $c^3$  by  $\frac{1}{2}c^3$  in front of  $N(\vec{\nu})N(\vec{\nu}')$ .

It can be shown<sup>2</sup> that  $\sigma d\Omega'$  takes the value